Cretaceous age, composition, and microstructure of pseudotachylyte in the Otago Schist, New Zealand

Running title: Pseudotachylyte in the Otago Schist

Shaun L.L. Barker[1*], Richard H. Sibson[1], J. Michael Palin,[1] John D. FitzGerald[2], Steve Reddy[3], Laurence N. Warr[4] and Ben A. van der Pluijm[5]

[1] Department of Geology, University of Otago, P.O. Box 56, Dunedin 9054, New Zealand

[2]Research School of Earth Sciences, The Australian National University, Canberra, ACT 0200, Australia

[3]The Institute for Geological Research, Department of Applied Geology, Curtin University of Technology, Perth, WA 6845, Australia

[4]Institute für Geographie und Geologie, Ernst Mortiz Arndt Universitaet Greifswald, Greifswald, Germany

[5]Department of Geological Sciences, University of Michigan, Ann Arbor, MI 48109-1005, U.S.A.

*Current address: Department of Earth and Ocean Sciences, University of British Columbia, Vancouver, BC V6T1Z4, Canada e-mail: sbarker@eos.ubc.ca

ABSTRACT

At Tucker Hill, in Central Otago, New Zealand, a series of pseudotachylyte veins are hosted in quartzofeldspathic schist. Chilled margins, microlites, flow banding, and the crystallisation of mineral phases absent from the host rock provide unequivocal evidence for melting during pseudotachylyte formation.

Whole rock analyses of pseudotachylyte reveal c. 3x enrichment of K_2O, Ba and Rb, and similar depletion of Na_2O, CaO, Sr and Eu, as compared to host schist. Formation age of pseudotachylyte is 95.9 ± 1.8 Ma as measured by total fusion $^{40}Ar/^{39}Ar$ analyses. Stepwise heating of pseudotachylyte matrix yields an excellently defined $^{40}Ar/^{39}Ar$ plateau age of 96.0 ± 0.3 Ma. These well-defined ages are attributed to the presence of potassium feldspar, low abundance of inherited lithic material from the host rock, and few fluid inclusions containing extraneous Ar. We propose that formation of these pseudotachylyte veins was related to Cretaceous extensional uplift and exhumation of the Otago Schist.

Keywords pseudotachylyte; schist; Otago; Ar-Ar; geochronology; friction melting

INTRODUCTION

The presence of pseudotachylyte (former friction melt) in a fault zone is commonly attributed to frictional melting of rock during seismic slip (Sibson 1975). As such, pseudotachylytes are valuable indicators that an exhumed fault zone was seismically active. Pseudotachylytes have been described from inactive, ancient fault zones (e.g. Outer Hebrides Fault Zone; Sibson 1975; Maddock 1983; Kelley et al. 1994) and present day seismically active fault zones (e.g. the Alpine Fault; Sibson et al. 1981; Bossiere 1991; Warr et al. 2003). Determining the formation age of pseudotachylyte can reveal when a fault was seismically active, and provide information on the significance of a pseudotachylyte-bearing fault zone relative to the timing of other regional deformation events (Kelley et al. 1994; Magloughlin et al. 2001; Sherlock & Hetzel 2001; Mueller et al. 2002; Warr et al. 2003).

In Central Otago, New Zealand, a series of pseudotachylyte veins are found in schist outcropping on Tucker Hill (169° 24'23"E; 45° 15'16"S), near the township of Alexandra (Fig. 1). The pseudotachylyte veins are hosted in the garnet-biotite-albite zone of the greenschist facies of the Otago Schist, which forms the basement rocks of much of the Otago region (Mortimer 1993a,b). Tucker Hill is approximately 15 km to the east of the Cromwell Gorge Shear Zone, and approximately 20 km to the south of the Rise and Shine Shear Zone, which are two Cretaceous age extensional shear zones (Deckert et al. 2002).

59 Previous studies that have attempted to determine the age of pseudotachylyte
60 utilizing $^{40}Ar/^{39}Ar$ geochronology in various localities have met with varying degrees of
61 success. In particular, accurate and geologically meaningful $^{40}Ar/^{39}Ar$ age determinations
62 are negatively influenced by the presence of variable amounts of inherited crystals (i.e.
63 incompletely melted) from host rocks (Magloughlin et al. 2001, Warr et al. 2007), argon
64 loss by diffusion or alteration (Davidson et al. 2003) or excess Ar in fluid inclusions (Di
65 Vincenzo et al. 2004).

66 In this study, we document the petrography and geochemistry of
67 pseudotachylyte veins, and present evidence for the origin of these pseudotachylyte
68 veins as a friction melt. In addition, we report laser ablation $^{40}Ar/^{39}Ar$ total fusion, single-
69 step infra-red laser heating ages, and stepwise heated $^{40}Ar/^{39}Ar$ analyses of fragments of
70 pseudotachylyte matrix. Our results demonstrate excellent agreement between both total
71 fusion and stepwise heating $^{40}Ar/^{39}Ar$ geochronology, which is attributed to the presence
72 of potassium feldspar as the likely host for the majority of argon, a lack of inherited lithic
73 material from the host rock, and no significant alteration of the material selected for
74 $^{40}Ar/^{39}Ar$ analysis.

75

76 GEOLOGICAL SETTING

77 The structural setting of the pseudotachylyte veins at Tucker Hill is described in
78 Barker (2005). Briefly, more than 100 pseudotachylyte veins are distributed throughout
79 several cataclastic fault zones. The largest of these fault zones occurs in shattered and
80 incoherent schist and is > 400 m long, c. 5-10 m thick, and dips gently east with an

unknown sense of displacement (Fig. 1D). In addition, several other pseudotachylyte-bearing fault zones were mapped that strike NNW and dip east. The majority of pseudotachylyte veins lie subparallel to schist foliation (Figs. 1, 2), and dip gently towards the northeast. The length of fault veins is highly variable, with most being between 1 and 10 m long, and < 2 cm thick. Slip-sense indicators, in the context of the veins present orientations, suggest that most veins have a top-to-the-north, normal sense of shear.

The beginning of regional metamorphism for the Otago Schist has been inferred at c. 199 Ma (Adams et al. 1985). Mortimer & Cooper (2004) suggest that the timing of highest grade metamorphic mineral growth in the Otago Schist was during the Jurassic. Little et al. (1999) inferred that peak metamorphism in the Otago Schist occurred in the middle Jurassic (170-180 Ma), and that the Otago Schist was held at mid to lower crustal depths until 135 Ma. Thereafter, exhumation occurred at 0.6–1 mm/yr (Little et al. 1999). Uplift and exhumation of the schist was accompanied by regional extension and the development of low-angle ductile shear zones at 135-105 Ma (Deckert et al. 2002; Forster & Lister 2003). Continuing extension in the mid Cretaceous led to the development of brittle normal faults with a NW/SE and NE/SW oriented orthogonal pattern (Craw & Norris 1991). Overlying volcanic sediments suggest that deep levels of the Otago Schist had been exposed by the mid-late Cretaceous (Adams & Raine, 1988). Neither the Rise and Shine Shear Zone, nor the Cromwell Gorge Shear Zone displace the Waipounamu Erosion Surface (LeMasurier & Landis, 1996), suggesting that shear zone displacement was complete by 105-85 Ma.

Pseudotachylyte veins at Tucker Hill do not appear to have any metamorphic overprint, and they crosscut all metamorphic fabrics. The oldest apatite fission track ages from a

105 nearby area (Tippett & Kamp 1993) suggest that these rocks were near the surface by c. 96–
106 86 Ma. Thus, a geologically reasonable age for pseudotachylyte formation is considered to
107 lie between 135 and 85 Ma.

108 Several thick pseudotachylyte veins were collected in the field, and three with
109 unequivocal evidence for melting (e.g., chill margins) were selected for geochemical
110 analysis (those rejected showed evidence for cataclasis, or were too small to provide
111 enough material for geochemical analyses). These 3 veins (samples University of Otago
112 reference numbers OU74171, OU 74172, OU 74178, housed in the Department of
113 Geology collection, University of Otago) were crushed and analysed for bulk rock by
114 X-ray fluorescence (XRF) and laser ablation inductively coupled plasma mass
115 spectrometry (LA-ICP-MS). Additionally, Ar-Ar geochronology was performed both on
116 an intact-rock section (laser ablation) and selected fragments (stepwise heating) of
117 OU74171. Nine host schist samples were also chosen from the Tucker Hill field area for
118 chemical comparison with pseudotachylyte. Fresh samples of schist were chosen, that is
119 rocks with no macroscopic or microscopic evidence for alteration.

120 ANALYTICAL METHODS

121 **XRF**

122 Wall rock was trimmed from the edges of pseudotachylyte veins using a
123 diamond saw and grindstone, and the veins were then crushed in a tungsten carbide
124 swing mill. Resulting powders were then turned into fused discs for major element
125 analysis. Trace element analyses were carried out on pressed powder discs, using the
126 procedures of Norrish and Chappell (1967), and checked for accuracy using a subset of
127 international standards (Govindavaju 1994). Analyses were conducted on a Phillips

PW-2400 Automated Sequential XRF Spectrometer in the Department of Geology, University of Otago.

LA-ICP-MS

One pseudotachylyte sample (OU 74171) and its adjacent host rock (OU 74179) were chosen for LA-ICP-MS analysis. These samples were crushed in an agate swing mill and then fused into glass. Analyses were carried out on an Agilent 7500 quadrupole ICP-MS at the Research School of Earth Sciences, The Australian National University. A pulsed Lambola Physik LPX 1201 ArF excimer laser operated at a constant energy, and a 5 Hz pulse rate was used to ablate material from the surface of the whole rock glass discs. A laser spot width of 70 μm was used during spot analyses of schist and pseudotachylyte fused whole rock samples.

Data reduction followed established protocols for time-resolved analysis (Longerich et al., 1996), using SiO_2 as an internal standard. Concentrations of SiO_2 determined by XRF analyses for schist and pseudotachylyte were used for LA-ICP-MS data reduction. The NIST 612 standard (values of Pearce et al. 1997) was analysed before and after every six analyses for standardisation.

Electron microscopy

One transmission electron microscope (TEM) specimen was prepared using standard petrographic thin section techniques, leading to extraction of a 3 mm diameter disc of rock and Argon-ion milling. Thin regions were dominantly found in the chlorite-rich matrix areas of the specimen. Transmission electron microscope observations were made at 300 kV using a Philips CM300 TEM (1999) based at the Research School of

151 Earth Sciences, The Australian National University. Scanning electron microscope
152 (SEM) observations on polished specimens were made on a Cambridge S360 SEM
153 (1987) in the Electron Microscope Unit, The Australian National University.

154 A whole rock powder X-ray diffraction (XRD) analysis was carried out on one
155 pseudotachylyte vein. X-ray diffraction was carried out with a SIEMENS D5005 Bragg-
156 Brentano diffractometer based in the Department of Geology, The Australian National
157 University.

158 **Ar-Ar geochronology**

159 For laser ablation Ar-Ar geochronology, a thin section of pseudotachylyte was
160 examined, and an area of matrix chosen and marked for analysis (e.g., an area free of
161 lithic clasts). The sample was wrapped in aluminium foil and loaded into an aluminium
162 package along with biotite age standard HD-B1 (24.21 ± 0.32 Ma) to monitor the
163 neutron flux gradient of the reactor (McMaster University Nuclear Reactor, Hamilton,
164 Canada).

165 Argon analyses were undertaken at the Western Australian Argon Isotope Facility,
166 Curtin University of Technology, Perth. Argon data were collected by single step, total
167 fusion infra-red laser heating of the thick polished pseudotachylyte sample. A 110 W
168 Spectron Laser Systems (CW-Nd-YAG laser (λ = 1064 nm) was used to fuse individual
169 c. 50 μm spots of the fault rock sample. Laser analyses were attempted from fine-
170 grained, clast-free areas of pseudotachylyte matrix. Gases released by fusion were
171 released into a high sensitivity mass spectrometer (MAP 215-50). Data were corrected
172 for mass spectrometer discrimination and nuclear interference reactions. The J value for

173 the irradiation was 0.003565 ± 0.000018. $^{40}Ar/^{39}Ar$ ages were calculated using the decay
174 constant of Steiger & Jaeger (1977).

175 For "intact rock" stepwise heating $^{40}Ar/^{39}Ar$ analysis, selected fragments of
176 pseudotachylyte matrix were irradiated in the McMaster Nuclear Reactor (Canada).
177 Unencapsulated samples were wrapped in aluminium foil and loaded into fused silica
178 tubing for neutron irradiation. Encapsulated samples were analysed using the method
179 described in Dong et al. (1995). The encapsulated samples were placed into fused silica
180 breakseal tubes that were subsequently evacuated to c. 5 x 10^{-8} Torr. The connections to
181 the breakseals were then collapsed while under vacuum. After neutron irradiation, the
182 capsules were placed into a glass manifold connected to the VG1200S mass spectrometer at
183 the University of Michigan. Upon breaking the fused silica vials, the recoil gas fraction can
184 be analysed on the mass spectrometer. All samples were step-heated using the defocused beam
185 from a 5W argon-ion continuous laser, and the ages quoted are relative to an age of 27.99
186 Ma for standard biotite FCT-3, which in turn is relative to an age of 520.4 Ma for a
187 standard hornblende MMhb-1 (Hall & Farrell 1995).

188 SAMPLE DESCRIPTIONS

189 **Host schist petrography**

190 Schist (Fig. 2A) can be separated into two dominant lithologic components -
191 quartz segregation bands and melanocratic bands. Segregation bands are composed of
192 large, moderately to highly strained quartz grains, with minor albitic plagioclase, and
193 rare muscovite, epidote and chlorite. Melanocratic bands have a larger proportion of
194 plagioclase than quartz segregation bands, with muscovite, chlorite and epidote also

present. More rarely, titanite (both metamorphic and relict detrital grains), detrital zircon, apatite, and tourmaline are observed in melanocratic bands. Long, dusty streaks of fine-grained graphite occur in all schist thin sections.

Pseudotachylyte petrography

Macroscopically, lithic clasts of quartz (and minor schist) up to 5 mm are present within pseudotachylyte veins. Dark margins are noticeable at the edges of many thick pseudotachylyte veins, and one thick vein shows evidence for repeated melt episodes, with multiple sets of dark margins, and mutual crosscutting relations (Fig. 2). Three components dominate the pseudotachylyte. These are: (1) lithic clasts; remnant mineral and rock fragments from schist (Fig. 2C) (2) grains that crystallised from the pseudotachylyte melt, which can be resolved by optical microscopy (>2 μm; Fig. 2C) and (3) fine-grained matrix (≤2 μm).

Most lithic clasts within the pseudotachylytes are quartz grains or aggregates, and are variable in size (2 μm to greater than 1 mm). Quartz lithic clasts are scattered relatively uniformly throughout thin fault veins. In thick veins, quartz lithic clasts are most abundant within the dark margins. Small quartz clasts (< 100 μm) are usually well rounded and intact. Larger quartz clasts are commonly more angular and contain fractures, some of which are filled with melt (Fig. 3A). Some quartz clasts display diffuse rims in both optical light microscopy and SEM (Fig. 3B). Small quartz clasts (<10 μm) are more commonly affected by such rims than larger quartz grains. Quartz lithic clasts show rare embayments where melt has intruded them. Plagioclase (Fig. 3C), is a minor lithic clast in the pseudotachylytes compared to quartz, and its modal proportion is estimated to be <1% of total pseudotachylyte volume

Small (typically 1-5 μm wide, 10-50 μm long), tabular crystals of potassium feldspar (characteristic XRD peaks at 3.22, 3.26, and 3.27 Å) occur in pseudotachylyte veins ≥0.5 cm in width. Potassium feldspar microlites are absent in the chill margins of veins, and become more abundant towards the centres of veins (Fig. 1C, confirmed by electron diffraction in TEM). Measurements made using EDS via the TEM suggest that the chemistry of potassium feldspar crystals changes little throughout the pseudotachylyte. Many quartz and plagioclase lithic clasts are radially overgrown by potassium feldspar microlites, and potassium feldspar infills small fractures in plagioclase lithic clasts.

Chlorite forms the majority of matrix material between potassium feldspar microlites (Figs. 3B, 3C, 4, 5). Selected area electron diffraction of chlorite reveals characteristic lattice spacing of 14 Å. Ultra-fine grained chlorite occurs as sharp, tabular crystals, which are typically 50-100 nm wide, and 1-2 μm long (Fig. 4, confirmed by electron diffraction in TEM). We suggest that the chlorite crystallised from a former glassy matrix.

Spherical structures, here referred to as spheroids, are found in all thick pseudotachylyte veins examined during this study. These spheroids range from 10-300 μm in diameter. Spheroids are not found in the dark margins of veins, and are larger and more numerous towards the centre of veins. Spheroids are filled with a consistent mineral assemblage comprising quartz, titanite ± potassium feldspar ± chlorite (Fig. 5A). Graphite is present in many of the spheroids, and occurs as a thin opaque (c. 1 μm) rim. Chlorite occurs as low relief, light green plates, and is often found projecting from the rim towards the centre of the spheroid. Titanite grains in spheroids grow to a relatively large size (up to 50 μm), and often have a radial, zoned appearance (Figs. 5B

242 and 5C). The spheroids have similarities to amygdules in pseudotachylytes described by
243 Maddock et al. (1987).

244 RESULTS

245 **Geochemistry**

246 Results obtained for whole rock major oxide XRF analyses of host schist and
247 pseudotachylyte are presented in Table 1. Fe_2O_3, MgO, CaO, Na_2O, and K_2O show
248 greater concentration variability between schist samples than SiO_2, TiO_2 and Al_2O_3.
249 Greater variation for these elements is likely due to minor variations in mineral content
250 (e.g., muscovite, chlorite, plagioclase) between schist samples. Sample OU 74185 has a
251 higher SiO_2 content (66%), with a higher content of quartz segregation bands diluting
252 concentrations of other elements. Major and trace element compositions of Tucker Hill
253 schist agree well with those of schists previously analysed from Alexandra by Mortimer
254 & Roser (1992).

255 Whole rock XRF results reveal that the pseudotachylyte and schist samples have
256 approximately the same SiO_2, Al_2O_3 Fe_2O_3 and MgO concentrations (Fig. 6A). CaO and
257 Na_2O contents are significantly lower in pseudotachylyte samples than they are in the
258 schist samples, while K_2O is higher in pseudotachylyte. The trace elements Sc, V, Cr,
259 Ni, Cu, Zn, Ga, As, Rb, Sr, Y, Zr, Nb, Ba, La, Ce, Nd, Pb, Th and U were analysed by
260 XRF, and are presented in Table 2 (Fig. 6B). The most notable differences between
261 pseudotachylyte and schist are the increases in Ba and Rb concentrations, and the
262 decrease in Sr, Ga, As and Y in pseudotachylyte as compared to the host schist. The
263 trace elements Sc, V, Cr, Co, Ni, Cu, Rb, Sr, Y, Zr, Nb, Cs, Ba, La, Ce, Pr, Nd, Sm, Eu,
264 Gd, Tb, Dy, Er, Yb, Lu, Ta, Pb, Th and U were determined by LA-ICP-MS on whole

rock glasses. The results for these analyses are presented in Table 3, with pseudotachylyte/schist ratios summarised in Figure 7A. Note that R, the ratio of the average concentration of an element in schist and pseudotachylyte is calculated by:

$$R = \frac{\text{pseudotachylyte concentration}}{\text{schist concentration}}$$

then the error (e) associated with R is:

$$e = R \times \left(\left(\frac{\text{pseudotachylyte SD}}{\text{pseudotachylyte } \bar{x} \text{ concentration}} \right)^2 + \left(\frac{\text{schist SD}}{\text{schist } \bar{x} \text{ concentration}} \right)^2 \right)^{0.5},$$

where SD= standard deviation of all analyses. Values of R (shown in Fig. 7) greater than 1 indicate enrichment of an element in pseudotachylyte relative to schist, values less than 1 indicate depletion of an element in pseudotachylyte relative to schist.

The results obtained by LA-ICP-MS agree well with those obtained by XRF. Notably, Eu is lower by a factor of 3 in pseudotachylyte. A plot showing rare earth element (REE) concentrations normalised to chondrite (values of McDonough & Sun 1995) demonstrates that schist and pseudotachylyte have almost identical REE patterns, excepting Eu which shows a marked negative anomaly in pseudotachylyte (Fig. 7B).

4.2 Ar-Ar geochronology

Argon release spectra for both samples (encapsulated and unencapsulated) show comparable degassing curves (Fig. 8). Minor disturbances during the release of ^{39}Ar occur at low temperatures, followed by the formation of a plateau. The small (0.0008 g) encapsulated fragment gave a total gas age of 95.95 Ma (Table 5), and had a small amount of recoiled ^{39}Ar (1.1 %). Variable and younger ages at low gas release temperatures

285 are associated with higher Cl/K and Ca/K (Fig. 8A). The remaining ~ 85% of degassed
286 ^{39}Ar forms a plateau at c. 96 Ma. At higher temperatures (final 10% of ^{39}Ar gas
287 released) fluctuating Cl/K and Ca/K are observed, but are not associated with strong
288 variations in calculated ages.

289 A larger sample (not encapsulated) produced an excellent ^{40}Ar/^{39}Ar plateau age of
290 95.85 ±0.70 Ma, which is defined by ca. 75% of degassed ^{39}Ar (Table 6). A similar total gas
291 age of 95.44 ±0.17 Ma is determined (Fig. 8B; see Table 5). In detail, the stepwise release
292 of the ^{39}Ar gas fraction shows minor disturbance for the first 12 steps of heating, with slightly
293 younger ages recorded for the first 30% of gas release. The first three steps produced
294 significantly younger ages of <85 Ma, and are associated with elevated Cl/K and Ca/K,
295 with younger ages having higher ratios. All other points of the spectrum show no
296 relationship between age and Cl/K or Ca/K. The average values for Cl/K and Ca/K are
297 notably low for this sample (0.074 and 0.00045, respectively).

298 For total-fusion Ar-Ar dating using laser ablation, twenty separate analyses were
299 attempted on one thin section. Of these, all but three analyses were abandoned because of
300 hydrocarbon interferences of unknown origin. The three completed analyses yield an
301 unweighted mean age of 95.8 ±1.8 Ma (Table 4).

302

303 DISCUSSION

304 **Pseudotachylyte Melt Origin and Emplacement**

305 Melting during pseudotachylyte formation is indicated by the presence of newly
306 crystallised phases, which are not found in the host schist (e.g. potassium feldspar),
307 igneous textures (e.g. fine-grained microlites and chilled margins) and the presence of

308 embayed lithic clasts. The most abundant newly crystallised phase found in the Tucker
309 Hill pseudotachylyte is potassium feldspar. Potassium feldspar has not been reported
310 from the Otago Schist, either as a metamorphic mineral, or contained within mineralised
311 veins (Youngson & Craw 1993). Thus, the presence of potassium feldspar in
312 pseudotachylyte is strong evidence for the formation and crystallisation of a melt, as it
313 cannot have been inherited as a lithic clast from the host schist.

314 In hand specimens, the outer margin of most thick (>0.5 cm) veins has a thin
315 (0.5 to 1 mm) black zone. When viewed in thin section, this margin is darker than the
316 inner area of the vein, contains no microlites, and very rare spheroids. We suggest that
317 these dark layers are chill margins that formed when melt produced during
318 pseudotachylyte formation was rapidly cooled against the vein wall. The chill margins
319 indicate that the cooling times of the veins were sufficiently long to generate a
320 temperature gradient across the vein, with material nearer the middle of veins cooling
321 slowly enough so that potassium feldspar microlites could nucleate and grow. Several
322 previous workers (e.g. Sibson 1975; Maddock 1983) consider chill margins to be a
323 strong indicator for the former presence of melt. Thin pseudotachylyte veins (<0.5 cm)
324 show no evidence for chill margins or the presence of potassium feldspar microlites.
325 This suggests that these thinner veins cool more quickly, with no opportunity for chill
326 margin development.

327 In several pseudotachylyte fault veins, lithic clasts show evidence for flow alignment,
328 with the long axes of quartz lithic clasts aligned subparallel to the walls of the
329 pseudotachylyte veins. This preferential alignment of lithic clasts suggests that there
330 was flow along veins during pseudotachylyte formation. In addition, macroscopic flow
331 banding has been noted in some pseudotachylyte veins (Fig. 9). Flow banding and

aligned lithic clasts suggest that friction melt viscosities were low enough (and cooling times long enough) to allow melt to flow along veins. Injection veins (e.g., non-shear surfaces) also require highly mobile melts, which can be rapidly injected from the generating (shear) surface into the injection vein (Sibson 1975).

Pseudotachylyte geochemistry

Pseudotachylyte compositions will be dependent on the mineralogy (and mineral chemistry) of the host rock, the pressure-temperature-volatile conditions attained during the melting process, and possible mineral-melt separation processes. The pseudotachylyte samples selected for analysis were separated by metres laterally and vertically. Thus, there is little chance that they came from a single fault surface. However, the similarity of pseudotachylyte compositions suggests that similar melting conditions applied to each pseudotachylyte-generating event.

The major and trace elements most enriched in the pseudotachylyte, namely K_2O, Rb and Ba, have similar petrochemical behaviours which are distinct from those most depleted in the pseudotachylyte (CaO, Na_2O and Sr). Petrographic observations suggest that the mineral in the schist most likely to contain significant concentrations of K_2O, Ba and Rb is muscovite (NB – no biotite or potassium feldspar is present in the host schist), implying that muscovite has been preferentially incorporated into pseudotachylyte during friction melting (*cf*. Kelley et al. 1994). The mineral most likely to contain significant concentrations of Na_2O, CaO, Sr and Eu is plagioclase. O'Hara (1992) also found pseudotachylyte veins with markedly increased K_2O, and attributed this increase to preferential melting of potassium-bearing minerals, in that case alkali feldspar. The results outlined above are consistent with both experimental work (Spray 1987; Spray 1988; Spray 1990; Spray 1995) and geochemical analyses of

356 pseudotachylyte from impact craters (Killick, 1994; Thompson and Spray, 1996) and
357 fault-hosted pseudotachylyte (Maddock 1992; Magloughlin 1992; O'Hara 1992;
358 Camacho et al. 1995; O'Hara and Sharp 2001). These previous studies suggested that
359 the formation of pseudotachylyte is accomplished by the preferential melting of hydrous
360 phases (e.g. micas, amphibole), and the preferential retention, as lithic clasts, of
361 plagioclase and quartz. The whole rock geochemical results from this study demonstrate
362 that there was preferential inclusion of a K-Rb-Ba bearing phase(s) and preferential
363 exclusion of a Ca-Na-Sr-Eu bearing phase(s) during pseudotachylyte formation. The
364 depletion of Sr and Eu strongly suggest that the phase depleted from the
365 pseudotachylyte is plagioclase, and not another Ca-bearing phase (i.e., epidote, which
366 may have a negative Eu anomaly; Harlavan and Erel, 2002).

367 An alternative explanation for the pseudotachylyte composition is seritization of schist
368 host rock prior to pseudotachylyte formation. Seritization would cause enrichment of
369 K_2O, and depletion of Na_2O and CaO. Studies of mid-ocean ridge hydrothermal systems
370 have established that mobilisation of REE occurs during such reactions, and a
371 pronounced positive Eu anomaly was observed in these hydrothermal solutions
372 (Douville et al. 2002). Therefore, it is possible that hydrothermal alteration could have
373 caused the geochemical differences observed between pseudotachylyte and unaltered
374 host schist. However, a significant amount of potassium metasomatism would have to
375 occur to cause the c. 4 times increase in potassium concentrations observed (*cf*. average
376 schist). Whereas there is clear field evidence for hydrothermal alteration (quartz and
377 calcite veins) crosscutting pseudotachylyte in some parts of the field area, it is unclear
378 whether any hydrothermal alteration of schist occurred prior to pseudotachylyte
379 formation.

Ar-Ar geochronology

The two Ar-Ar geochronological methods yield statistically indistinguishable ages for the formation of this pseudotachylyte vein. The argon release spectra obtained from the stepwise heating method are excellent, and have more homogeneous plateaus than the results presented in Magloughlin et al. (2001) and Mueller et al. (2002). This may be because the principal potassium-bearing phase in this sample is potassium feldspar, and the sample contains no biotite. Additionally, the sample appears to have few lithic clasts other than quartz and plagioclase. Step-heating potassium feldspar is of particular value, because it remains stable during heating under vacuum to the onset of melting. This sample clearly has neither lost nor gained significant argon following the closure of the system, which is reflected in the plateau age. There is also little recoil of argon. A key feature of this sample is its potassium rich, Ca and Cl-poor nature. This implies a low abundance of fluid inclusions, which can contain extraneous argon. All of the above features make this pseudotachylyte vein an excellent candidate for Ar-Ar geochronology.

The advantages of combining both stepwise heating of matrix fragments, and laser ablation Ar-Ar techniques have been previously documented by both Magloughlin et al. (2001) and Mueller et al. (2002). These two techniques allow melt-related ages to be derived from potentially complex age spectra. Here, we have demonstrated that a potassic rich sample, containing little inherited host rock material (other than quartz and plagioclase) can produce smooth stepwise heating spectra with plateau and total gas ages that are indistinguishable from ages determined by laser ablation spot Ar-Ar analyses.

The ages determined for pseudotachylyte formation are geologically compatible with regional studies of the uplift and erosion of the Otago Schist belt. Previous studies have

403 documented the location and timing of ductile shear zone formation (Deckert et al. 2002;
404 Forster & Lister 2003), brittle fault formation (Craw & Norris 1991), cooling (Tippett &
405 Kamp 1993) and deposition of sedimentary rocks on top of the Otago Schist. Prior to this
406 study, the only direct evidence for faulting of late Cretaceous age in the Otago region
407 was in three areas where late Cretaceous sedimentary rocks are preserved; i.e., the
408 Kyeburn Formation, Henley Breccia and Horse Range Formation (Bishop & Laird,
409 1976; Bishop & Turnbull 1996, Forsyth, 2001). The Kyeburn and Horse Range
410 Formations have been interpreted as synorogenic sedimentary deposits, which contain
411 tuffs that yield ages of 112 Ma (Tulloch et al., in press).
412 We suggest that these pseudotachylyte veins were formed by seismic activity in the
413 upper Cretaceous (Cenomanian), and may be related to the latest stages of the uplift and
414 exhumation of the Otago Schist. These new age data provide unambiguous evidence for
415 Cretaceous faulting in the Otago Schist, with Ar-Ar geochronology specifically placing
416 the age of pseudotachylyte formation at 96 Ma. This study raises the possibility that
417 exhumation-related faults in the Otago Schist may be more widespread than previously
418 suspected.
419

420 ACKNOWLEDGMENTS

421 Nick Mortimer, Alan Cooper, Dave Craw, Doug Coombs, Stephen Cox have offered much
422 useful advice and discussion during this research. Brent Pooley and Harri Kokkonen are
423 thanked for assistance with petrographic preparation. This work was part of a BSc (Hons)
424 project by S. Barker conducted at the Department of Geology, University of Otago.
425 Barker acknowledges a summer research scholarship from The Australian National
426 University, during which much of this research was undertaken. This study was partially

427 funded by the Marsden Fund (Contract UOO 216-"Fault rock studies on seismic and
428 aseismic slip processes") administered by the Royal Society of New Zealand. The Ar-Ar
429 research (Michigan) was supported by grants from the U.S. National Earthquake Hazards
430 Reduction Program (USGS-04HQGR0066) and the U.S. National Science Foundation (EAR-
431 0230055 and 0345985).
432
433 REFERENCES

434 Adams C, Bishop D, Gabites J 1985. Potassium-argon age studies of a low-grade,
435 progresively metamorphosed greywacke sequence, Dansey Pass, New Zealand. Journal of
436 the Geological Society of London 142: 339– 349.

437 Adams C, Raine J 1988. Age of Cretaceous silicic volcanism at Kyeburn, central Otago,
438 and Palmerston, eastern Otago, South Island, New Zealand. New Zealand Journal of
439 Geology and Geophysics 31: 471–475.

440 Barker S. 2005 Pseudotachylyte-generating faults in Central Otago, New Zealand.
441 Tectonophysics 397: 211–223.

442 Bishop DG, Laird MG 1976. Stratigraphy and depositional environment of the Kyeburn
443 Formation (Cretaceous), a wedge of coarse terrestrial sediments in Central Otago.
444 Journal of the Royal Society of New Zealand 6: 55-71.

445 Bishop DG, Turnbull IM (compilers) 1996. Geology of the Dunedin area. Institute of
446 Geological & Nuclear Sciences 1:250 000 Geological Map 21. Institute of
447 Geological & Nuclear Sciences, Lower Hutt, New Zealand.

448 Bossiere G 1991. Petrology of pseudotachylytes from the Alpine Fault of New Zealand.
449 Tectonophysics 196: 173–193.
450 Camacho A., Vernon RH, Fitz Gerald JD 1995. Large volumes of anhydrous
451 pseudotachylyte in the Woodroffe Thrust, eastern Musgrave Ranges, Australia.
452 Journal of Structural Geology 17: 371-383.

453 Craw D, Norris R 1991. Metamorphogenic Au-W veins and regional tectonics;
454 mineralisation throughout the uplift history of the Haast Schist, New Zealand. New
455 Zealand Journal of Geology and Geophysics 34: 373–383.

456 Davidson C, Davis KJ, Bailey CM, Tape CH, Singleton J, Singer B 2003. Age, origin,
457 and significance of brittle faulting and pseudotachylyte along the Coast shear zone,
458 Prince Rupert, British Columbia. Geology 31: 43-46

459 Deckert H, Ring U, Mortimer N 2002. Tectonic significance of Cretacoues bivergent
460 extensional shear zones in the Torlesse accretionary wedge, central Otago Schist, New
461 Zealand. New Zealand Journal of Geology and Geophysics 34: 373–383.

462 Di Vincenzo G, Rocchi S, Rossetti F, Storti F 2004. ^{40}Ar-^{39}Ar dating of
463 pseudotachylytes: the effect of clast-hosted extraneous argon in Cenozoic fault-
464 generated friction melts from the West Antarctic Rift System. Earth and Planetary
465 Science Letters 223: 349-364

466 Dong H, Hall C, Peacor D, Halliday A 1995. Mechanisms of argon retention in clays
467 revealed by laser ^{40}Ar/^{39}Ar dating. Science 267: 355–359.

468 Douville E, Charlou L, Oelkers EH, Bienvenu P, Jove Colon CF, Donval JP, Fouquet
469 Y, Prieur D, Appriou P 2002. The Rainbow Vent fluids (36 degrees 14'N,
470 MAR); the influence of ultramafic rocks and phase separation on trace metal
471 content in Mid-Atlantic Ridge hydrothermal fluids. Chemical Geology 184: 37-
472 48.
473 Forster M, Lister G 2003. Cretaceous metamorphic core complexes in the Otago Schist,
474 New Zealand. Australian Journal of Earth Sciences 50: 181–198.
475 Forsyth PJ (compiler) 2001. Geology of the Waitaki area. Institute of Geological &
476 Nuclear Sciences 1:250 000 Geological Map 19. Institute of Geological & Nuclear
477 Sciences, Lower Hutt, New Zealand.
478 Govindavaju KA 1994. A 1994 Compilation of working values and sample description
479 for 383 geostandards. Geostandards Newsletter, 1: 158.

480 Hall C, & Farrell J 1995. Laser $^{40}Ar/^{39}Ar$ ages of tephra from Indian Ocean deep-sea
481 sediments; tie points for the astronomical and geomagnetic polarity time scales. Earth and
482 Planetary Science Letters 133: 327– 338.
483 Harlavan Y, Erel Y 2002. The release of Pb and REE from granitoids by the dissolution
484 of accessory phases. Geochimica et Cosmochimica Acta 66: 837-848.

485 Kelley S, Reddy S, Maddock R 1994. Laser-probe $^{40}Ar/^{39}Ar$ investigation of a
486 pseudotachylyte and its host rock from the Outer Isles Thrust, Scotland. Geology 22:
487 443–446.
488 Killick AM 1994. The geochemistry of pseudotachylyte and its host rocks from the
489 West Rand Goldfield, Witwatersrand Basin, South Africa; implications for
490 pseudotachylyte genesis. Lithos 32: 193-205.

491 LeMasurier W, Landis C 1996. Mantle-plume activity recorded by low-relief erosion
492 surfaces in West Antarctica and New Zealand. Geological Society of America Bulletin
493 108 (11), 1450–1466.

494 Little T, Mortimer N, McWilliams M 1999. An episodic Cretaceous cooling model for
495 the Otago-Marlborough Schist, New Zealand, based on $^{40}Ar/^{39}Ar$ white mica ages.
496 New Zealand Journal of Geology and Geophysics 42: 305–325.
497 Longerich H, Jackson S, Gunter D 1996. Laser ablation inductively coupled plasma mass
498 spectrometric transient signal data acquisition and analyte concentration calculation.
499 Journal of Analytical Atomic Spectrometry 11: 899–904.

500 Maddock R 1983. Melt origin of fault-generated pseudotachylytes demonstrated by
501 textures. Geology 11: 105–108.

502 Maddock R, Grocott J, van Nes M. 1987. Vesicles, amygdales and similar structures in
503 fault-generated pseudotachylytes. Lithos 20: 419–432.
504 Maddock RH 1992. Effects of lithology, cataclasis and melting on the composition of
505 fault-generated pseudotachylytes in Lewisian gneiss, Scotland. Tectonophysics
506 204: 261-278.
507 Magloughlin JF, Spray JG, 1992. Frictional melting processes and products in
508 geological materials; introduction and discussion. Tectonophysics 204: 197-204.

509 Magloughlin J, Hall C, van der Pluijm B 2001. $^{40}Ar/^{39}Ar$ geochronometry of
510 pseudotachylytes by vacuum encapsulation; North Cascade Mountains, Washington,
511 USA. Geology 29: 51–54.
512 McDonough WF, and Sun S 1995. The composition of the Earth. Chemical Geology
513 120: 223-253.

514 Mortimer, N. 1993a Geology of the Otago Schist and adjacent rocks. scale 1: 500 000.

515 Mortimer, N. 1993b Jurassic tectonic history of the Otago Schist, New Zealand.
516 Tectonics 12: 237–244.

517 Mortimer N, Cooper A 2004. U-Pb and Sm-Nd from the Alpine Schist, New Zealand.
518 New Zealand Journal of Geology and Geophysics 47: 21–28.

519 Mortimer N, Roser BP 1992. Geochemical evidence for the position of the Caples-
520 Torlesse boundary in the Otago Schist, New Zealand. Journal of the Geological
521 Society of London 149: 967-977.

522 Mueller W, Kelley S, Villa I 2002. Dating fault-generated pseudotachylytes; comparison
523 of $^{40}Ar/^{39}Ar$ stepwise-heating, laser-ablation and Rb-Sr microsampling analyses.
524 Contributions to Mineralogy and Petrology 144: 57–77.

525 Norrish, K. and Chappell, B., 1967. X-ray fluoresence spectrography. In: J. Zussman
526 (Editor), Physical Methods in Determinative Mineralogy. Academic Press, London,
527 pp. 161-214.

528 O'Hara, K., 1992. Major- and trace-element constraints on the petrogenesis of a fault-
529 related pseudotachylyte, western Blue Ridge Province, North Carolina.
530 Tectonophysics. 204: 279-288.

531 O'Hara KD, Sharp ZD 2001. Chemical and oxygen isotope composition of natural and
532 artificial pseudotachylyte; role of water during frictional fusion. Earth and
533 Planetary Science Letters 184: 393-406.

534 Pearce NJG, Perkins WT, Westgate JA, Gordon MP, Jackson SE, Neal CR, Chenery SP
535 1997. A compilation of new and published major and trace element data for NIST

536 SRM 610 and NIST SRM 612 glass reference materials. Geostandards and
537 Geoanalytical Research 21: 115-144

538 Sherlock S, Hetzel R 2001. A laser-probe $^{40}Ar/^{39}Ar$ study of pseudotachylite from the
539 Tambach fault zone, Kenya; direct isotopic dating of brittle faults. Journal of Structural
540 Geology 23: 33–44.

541 Sibson R. 1975 Generation of pseudotachylyte by ancient seismic faulting. The
542 Geophysical Journal of the Royal Astronomical Society 43: 775– 794.

543 Sibson R, White S, Atkinson B 1981. Structure and distribution of fault rocks in the
544 Alpine Fault Zone, New Zealand. In Thrust and nappe tectonics; International
545 conference. (ed. McClay & R. . Price), Special Publication - Geological Society of
546 London 9: 197–210

547 Spray JG 1987. Artificial generation of pseudotachylyte using friction welding
548 apparatus; simulation of melting on a fault plane. Journal of Structural Geology
549 9: 49-60.

550 Spray JG 1988. Generation and crystallization of an amphibole shear melt; an
551 investigation using radial friction welding apparatus. Contributions to
552 Mineralogy and Petrology 99: 464-475.

553 Spray JG, 1990. Experimental friction melting of Lewisian gneiss; implications for
554 Outer Hebrides thrust fault dynamics. In: Geological Society of America, 1990
555 annual meeting. Abstracts with Programs : 285-286.

556 Spray, J.G., 1993. Viscosity determinations of some frictionally generated silicate
557 melts; implications for fault zone rheology at high strain rates. Journal of
558 Geophysical Research 98: 8053-8068.

559 Spray JG 1995. Pseudotachylyte controversy; fact or friction? Geology 23: 1119-1122.

560 Steiger, R. & Jaeger, E. 1977 Subcommission on geochronology; convention on the use
561 of decay constants in geo- and cosmochronology. Earth and Planetary Science Letters
562 36: 359–362.

563 Thompson, LM, Spray JG 1996. Pseudotachylyte petrogenesis; constraints from the
564 Sudbury impact structure. Contributions to Mineralogy and Petrology 125: 359-
565 374.

566 Tippett J, Kamp P 1993. Fission track analysis of the late Ceno-zoic vertical kinematics
567 of continental pacific crust, Otago Schist, New Zealand. Journal of Geophysical
568 Research 98: 16,119–16,148.

569 Tulloch AJ, Ramezani J, Mortimer N, Mortensen J, van den Bogaard P, Maas R 2009.
570 Mid-Cretaceous felsic volcanism in New Zealand and Lord Howe Rise (Zealandia)
571 as a precursor to continental breakup. Geol Soc London Special Publication 321 in
572 press

573 Warr L, van der Pluijm B, Peacor D, Hall C. 2003 Frictional melt pulses during a
574 approximately 1.1 Ma earthquake along the Alpine Fault, New Zealand. Earth and
575 Planetary Science Letters 209: 39–52.

576 Warr L, van der Pluijm B, Tourscher S 2007. The age and depth of exhumed friction
577 melts along the Alpine Fault, New Zealand. Geology 35: 603-606.

578 Youngson JH, Craw D 1993. Gold nugget growth during tectonically induced
579 sedimentary recycling, Otago, New Zealand. Sedimentary Geology 84: 71-88.
580

Tables

Table 1: Major element (wt%) concentrations for schist and pseudotachylyte from XRF analyses.

Sample	SiO_2	TiO_2	Al_2O_3	$Fe_2O_3^t$	MnO	MgO	CaO	Na_2O	K_2O	P_2O_5	LOI	% Total
Schist 1 (OU74180)	59.34	0.90	17.47	7.39	0.11	3.11	2.87	2.69	2.79	0.22	3.14	100.03
Schist 2 (OU74181)	60.55	0.79	18.06	5.86	0.08	2.08	3.43	3.96	2.35	0.21	2.63	100.00
Schist 3 (OU74182)	58.90	0.80	17.85	6.96	0.08	2.08	3.25	3.08	2.76	0.25	3.33	99.34
Schist 4 (OU74183)	60.55	0.83	17.06	6.48	0.09	2.33	4.01	3.97	1.92	0.21	2.41	99.86
Schist 5 (OU74184)	59.88	0.90	17.02	7.03	0.10	2.80	4.01	3.79	1.63	0.21	2.71	100.08
Schist 6 (OU74185)	66.51	0.70	14.51	5.33	0.08	1.96	3.01	3.21	1.94	0.20	2.17	99.62
Schist 7 (OU74186)	60.60	0.85	16.96	6.64	0.09	2.60	3.94	3.80	1.68	0.19	2.52	99.87
Schist 8 (OU74187)	57.53	0.87	18.50	6.78	0.09	2.32	4.84	3.14	2.88	0.21	2.81	99.97
Schist 9 (OU74188)	61.39	0.78	16.92	6.17	0.09	2.18	4.01	4.09	1.72	0.21	2.45	100.01
Average	60.58	0.82	17.15	6.52	0.09	2.38	3.71	3.53	2.19	0.21	2.69	99.86
Standard Deviation	2.50	0.06	1.14	0.64	0.01	0.38	0.62	0.50	0.51	0.02	0.36	
Pst. 1 (OU 74171)	59.96	0.78	16.31	6.45	0.10	2.57	1.46	0.94	8.57	0.19	2.54	99.87
Pst. 2 (OU 74172)	58.54	0.78	16.58	6.33	0.10	2.50	1.81	0.86	9.39	0.19	2.77	99.85
Pst. 3 (OU 74178)	58.46	0.79	16.90	6.38	0.09	2.45	1.50	0.88	9.39	0.19	2.56	99.59
Average	58.99	0.78	16.60	6.39	0.10	2.51	1.59	0.89	9.12	0.19	2.62	99.77
Standard Deviation	0.84	0.01	0.30	0.06	0.01	0.06	0.19	0.04	0.47	0.00	0.13	

Table 2: Trace element (mg/kg) composition of schist and pseudotachylyte from XRF analyses.

Sample	Sc	V	Cr	Ni	Cu	Zn	Ga	As	Rb	Sr	Y	Zr	Nb	Ba	La	Ce	Nd	Pb	Th	U
Schist 1 (OU74180)	14	151	51	18	39	88	21	5	92	384	22	156	9	673	18	53	30	23	11	5
Schist 2 (OU74181)	13	133	43	16	20	80	20	7	81	401	22	176	8	558	18	45	23	16	11	4
Schist 3 (OU74182)	12	119	37	15	19	74	17	8	65	365	19	155	6	585	16	32	15	21	8	4
Schist 4 (OU74183)	16	152	52	18	27	82	19	10	63	491	21	162	7	541	15	40	19	17	7	3
Schist 5 (OU74184)	15	152	54	18	39	88	20	4	92	383	22	156	9	679	19	51	25	24	10	4
Schist 6 (OU74185)	17	170	52	19	25	83	19	17	53	471	19	149	7	512	22	36	23	14	8	3
Schist 7 (OU74186)	16	141	49	17	35	75	20	7	57	480	22	164	6	492	22	56	19	18	7	3
Schist 8 (OU74187)	16	155	44	15	44	72	22	8	84	591	22	172	9	699	17	47	20	17	9	4
Schist 9 (OU74188)	14	157	48	17	38	76	19	11	56	474	20	151	6	516	18	34	19	16	7	4
Average=	15	148	48	17	32	80	20	9	71	449	21	160	7	584	18	44	21	18	9	4
Pst. 1 (OU 74171)	12	131	37	18	32	76	13	5	209	270	13	152	9	1670	18	48	18	22	7	3
Pst. 2 (OU 74172)	14	126	37	18	32	74	13	5	226	260	12	148	10	1480	17	44	25	20	9	4
Pst. 3 (OU 74178)	14	135	38	18	40	76	13	4	215	237	13	145	12	2069	15	47	24	19	9	4
Average=	14	131	38	18	36	75	13	5	221	249	13	147	11	1775	16	46	25	20	9	4

Table 3: Trace element composition (mg/kg) of pseudotachylyte and schist whole rock glasses as determined by LA-ICP-MS, for separate spot analyses carried out on fused samples for elements Sc to La. Ce to U on following page.

Sample	SiO_2 (wt%)	Sc	V	Cr	Co	Ni	Cu	Rb	Sr	Y	Zr	Nb	Cs	Ba	La
Schist Glass 1a	60.6	22.2	165	41.3	13.9	13.7	16.0	57.8	551	24.3	179	7.1	2.6	464	24.8
Schist Glass 1b	60.6	17.0	136	32.5	11.0	10.7	14.5	64.6	440	18.4	133	6.3	3.6	392	19.3
Schist Glass 1c	60.6	22.4	172	44.5	15.4	14.9	19.9	60.8	542	24.7	191	7.5	3.2	462	25.8
Schist Glass 1d	60.6	21.2	137	38.1	10.7	10.6	13.3	66.2	506	23.4	154	6.6	3.7	439	24.3
Schist Glass 1e	60.6	21.3	164	41.7	12.0	12.3	14.2	67.7	533	23.7	160	8.3	3.8	459	24.7
Schist Glass 1f	60.6	20.5	161	40.4	13.6	13.6	20.0	64.9	545	23.4	182	7.7	3.6	472	25.0
Average=	60.6	20.7	156	39.7	12.7	12.6	16.3	63.7	520	23.0	166	7.3	3.4	448	24.0
Pseudotachylyte 2a	59	16.5	129	39.1	13.6	15.1	22.8	225	240	18.7	143	6.2	2.1	1840	18.2
Pseudotachylyte 2b	59	16.0	128	38.8	13.3	14.7	21.6	238	230	17.7	139	6.1	2.5	1790	17.5
Pseudotachylyte 2c	59	16.3	127	39.2	13.6	15.4	22.0	203	234	18.2	137	6.2	1.7	1810	17.7
Pseudotachylyte 2d	59	16.6	129	38.7	14.2	15.8	23.0	264	238	18.8	146	6.6	2.8	1860	18.4
Pseudotachylyte 2e	59	16.2	130	39.1	14.0	16.6	24.3	240	239	18.5	143	6.6	2.1	1900	18.4
Pseudotachylyte 2f	59	16.0	131	38.6	13.7	15.5	23.7	255	235	18.2	150	6.7	2.7	1900	18.8
Average=	59	16.2	129	38.9	13.7	15.5	22.9	237	236	18.4	143	6.4	2.3	1850	18.2

Table 3 (continued): Elements Ce to U

Sample	Ce	Pr	Nd	Sm	Eu	Gd	Tb	Dy	Er	Yb	Lu	Ta	Pb	Th	U
Schist Glass 1a	54.9	6.6	24.1	5.6	1.49	5.0	0.77	4.8	2.7	2.6	0.40	0.58	18.9	9.3	2.3
Schist Glass 1b	42.8	5.1	18.7	4.3	1.14	3.9	0.57	3.7	2.1	2.1	0.30	0.50	14.3	7.2	1.9
Schist Glass 1c	57.1	6.8	25.1	5.8	1.51	5.3	0.78	4.9	2.9	2.8	0.42	0.60	18.1	9.5	2.4
Schist Glass 1d	54.1	6.4	23.9	5.4	1.53	4.9	0.72	4.7	2.6	2.6	0.37	0.55	13.2	9.0	2.3
Schist Glass 1e	55.0	6.5	24.3	5.5	1.50	5.1	0.73	4.7	2.6	2.6	0.40	0.67	16.1	9.3	2.4
Schist Glass 1f	55.2	6.5	24.4	5.7	1.46	5.1	0.74	4.7	2.7	2.7	0.41	0.64	18.5	9.3	2.4
Average=	53.2	6.3	23.4	5.4	1.44	4.9	0.72	4.6	2.6	2.6	0.39	0.59	16.5	8.9	2.3
Pseudotachylyte 2a	42.3	5.1	18.9	4.3	0.47	4.1	0.57	3.6	2.1	2.1	0.32	0.50	22.8	7.9	1.8
Pseudotachylyte 2b	40.7	4.8	18.0	4.2	0.46	3.8	0.57	3.4	2.1	2.0	0.30	0.50	25.2	7.9	1.9
Pseudotachylyte 2c	41.3	4.9	18.6	4.4	0.48	4.0	0.57	3.7	2.1	2.1	0.33	0.50	16.6	8.1	1.9
Pseudotachylyte 2d	42.7	5.0	18.9	4.4	0.52	4.0	0.59	3.7	2.1	2.1	0.33	0.51	27.0	8.1	1.9
Pseudotachylyte 2e	42.8	5.1	19.0	4.4	0.51	4.0	0.60	3.8	2.1	2.2	0.33	0.53	27.5	8.2	1.9
Pseudotachylyte 2f	43.8	5.2	19.4	4.5	0.51	4.0	0.59	3.8	2.2	2.3	0.33	0.56	29.4	8.4	2.0
Average=	42.3	5.0	18.8	4.4	0.49	4.0	0.58	3.7	2.1	2.1	0.32	0.52	24.8	8.1	1.9

Table 4: Results from laser ablation Ar-Ar analyses.

Sample no.	$^{40}Ar/^{39}Ar$	±	$^{38}Ar/^{39}Ar$	±	$^{37}Ar/^{39}Ar$	±	$^{36}Ar/^{39}Ar$	±	^{39}Ar (cm^3)	±	$^{40}Ar^*/^{39}Ar$	±	Age (Ma)	±
OU74172-1	22.22036	0.04138	0.01719	0.00028	0.40077	0.15314	0.02199	0.00079	1.09E-11	1.65E-14	15.72151	0.23445	**98.4**	**1.5**
OU74172-2	23.91910	0.02996	0.01722	0.00021	0.50640	0.05374	0.02987	0.00033	1.48E-11	1.12E-14	15.09113	0.10128	**94.5**	**0.8**
OU74172-3	22.49993	0.05032	0.01711	0.00041	0.70186	0.10989	0.02494	0.00066	7.39E-12	6.06E-15	15.13125	0.20124	**94.8**	**1.3**
unweighted mean													95.9	1.8
weighted mean													95.2	0.6

Table 5: Data obtained for Ar-Ar dating during step-heating analysis of the encapsulated sample. Volumes are given in ccSTP/g x 10^{13} (i.e. a value of 1 in the table is actually 1 x 10^{-13}).

Fraction of Ar released	Laser Power (mW)	Vol ^{36}Ar	± (1σ)	Vol ^{37}Ar	± (1σ)	Vol ^{38}Ar	± (1σ)	Vol ^{39}Ar	± (1σ)	Vol ^{40}Ar	± (1σ)	Age(Ma)	± (1
0.011	0	4.86785	0.10338	1.53167	0.69153	2.61398	0.13002	14.07	0.16982	1447.96868	1.44904	0.60	
0.021	100	0.72678	0.11186	1.90734	0.36271	0.58111	0.09973	13.17973	0.11906	944.74103	1.97544	48.28	
0.043	200	0.26465	0.09042	1.82029	0.29862	0.32158	0.08629	28.9472	0.28293	3166.2912	2.5664	91.88	
0.082	300	0.18305	0.09767	3.85204	0.5506	0.00334	0.12325	52.08441	0.20068	4797.07015	1.64876	78.72	
0.142	400	0.50642	0.10526	4.79552	0.35921	0.24244	0.0967	78.22856	0.40913	8281.5017	4.20268	89.58	
0.206	500	0.27463	0.09286	2.45561	0.52627	0.0335	0.04878	84.32857	0.35917	10003.0092	4.52407	101.07	
0.262	600	0.20989	0.07165	1.81904	0.44048	0.0259	0.0636	74.53142	0.23625	8812.2104	3.74482	100.86	
0.360	800	0.52517	0.06088	2.86125	0.41913	0.29187	0.09619	129.01627	0.36723	14901.0319	9.3074	98.26	
0.434	1000	0.58995	0.06172	1.87928	0.35681	0.27262	0.08114	96.82226	0.46458	11371.75722	3.86627	99.39	
0.509	1200	0.55006	0.04857	2.56515	0.47836	0.1343	0.09912	99.44944	0.33001	11614.9105	4.5768	98.98	
0.695	1600	1.07355	0.07464	8.96223	0.43737	0.17918	0.11616	244.82848	0.5746	28292.0098	8.86116	98.23	
0.793	2000	1.35412	0.09827	7.19814	0.41631	0.26161	0.07999	129.55478	0.49909	15224.82431	4.83844	98.37	
0.858	2600	2.488	0.08489	4.52576	0.34998	0.49672	0.06701	85.70744	0.2797	10645.43612	4.73853	99.38	
0.892	3200	3.58435	0.07314	2.73909	0.23195	0.97403	0.12971	43.99144	0.29654	6139.06287	3.90172	99.25	
0.934	4000	5.79711	0.12994	5.04798	0.36572	1.25278	0.07151	56.25585	0.21593	8107.38338	3.94338	97.73	
0.953	4010	2.92327	0.14589	2.26677	0.41881	0.60125	0.0925	24.77163	0.21649	3739.4048	2.59707	99.76	
1.000	4020	3.49704	0.17447	10.89659	0.59325	0.79792	0.07835	61.75511	0.46845	8167.39605	3.20318	99.29	

Table 6: Data obtained for Ar-Ar dating during step-heating analysis of the non-encapsualted sample. Volumes are given in ccSTP/g x 10^{13} (i.e. a value of 1 in the table is actually 1 x 10^{-13}).

Fraction of Ar released	Laser Power (mW)	Vol ^{36}Ar	± (1σ)	Vol ^{37}Ar	± (1σ)	Vol ^{38}Ar	± (1σ)	Vol ^{39}Ar	± (1σ)	Vol ^{40}Ar	± (1σ)	Age(Ma)	± (
0.003388	100	1.17422	0.09054	2.46271	0.17798	0.56443	0.08181	36.23806	0.19863	3018.73801	1.72291	64.11	
0.0142252	200	3.16186	0.11307	7.63095	0.3863	1.09217	0.06468	115.91281	0.43299	12243.2712	5.12109	84.36	
0.0346589	300	3.13885	0.09402	11.73883	0.34655	1.35342	0.08781	218.55588	0.77563	22304.99056	7.29883	84.57	
0.0664335	400	2.84413	0.07284	13.30712	0.45995	1.28363	0.15512	339.85743	0.65152	37227.86944	8.30107	92.37	
0.088674	450	0.83659	0.0952	6.78716	0.48022	0.54799	0.08867	237.88124	0.45605	26871.29045	8.2036	96.44	
0.1085274	500	0.97111	0.13149	6.04018	0.27997	0.38115	0.13604	212.34945	0.47489	23946.24375	7.74434	96.02	
0.1295684	550	1.14271	0.15888	7.36958	0.26705	0.48501	0.09573	225.05163	0.64555	25011.95681	5.3068	94.53	
0.1561213	600	1.07519	0.12022	8.42832	0.34506	0.8343	0.17522	284.00549	0.70347	31151.49165	10.5412	93.63	
0.1833262	650	1.16536	0.11984	7.47219	0.33256	0.5198	0.07809	290.97979	0.75065	32052.60007	8.84918	93.97	
0.2118509	700	1.3337	0.16541	7.83143	0.4029	0.95498	0.15687	305.0966	0.7813	33572.45047	14.98777	93.78	
0.249493	800	0.85143	0.09144	9.13227	0.33249	0.69112	0.11369	402.61544	0.99543	44695.71218	13.70752	95.16	
0.2922827	900	1.05937	0.09173	9.79527	0.25441	0.79516	0.1315	457.67298	0.70162	51271.56895	9.38939	95.96	
0.3390644	1000	0.69024	0.13326	10.26425	0.33742	0.74739	0.14254	500.37027	0.74099	56261.17449	10.33395	96.54	
0.4276407	1200	1.95553	0.07377	24.88465	0.40069	1.46673	0.16807	947.40014	1.15628	106559.79	43.55017	96.40	
0.5288433	1400	2.05611	0.14324	39.37147	0.28642	1.88447	0.21467	1082.44924	0.82355	121872.927	36.57543	96.53	
0.627053	1600	2.66876	0.13101	48.75395	0.63955	1.55786	0.25505	1050.43769	0.94685	118466.6658	54.46014	96.53	
0.7589846	2000	4.3451	0.12037	101.41511	0.60856	2.57855	0.28954	1411.12283	1.60021	159035.6385	63.34881	96.33	
0.9000545	3000	4.95408	0.17566	104.71699	0.76232	2.96269	0.15118	1508.86507	2.24813	169683.8045	61.95527	96.08	
1	4000	4.01146	0.12102	55.55436	0.57939	2.39106	0.2121	1069.00308	2.13066	120716.1471	44.16197	96.35	

Figure Captions

Fig. 1: (A) Map of New Zealand showing the location of Tucker Hill (B) Map of section of the South Island of New Zealand showing the location of Tucker Hill relative to key geographical features, and the location of the Cromwell Gorge Shear Zone (CGSZ), Rise and Shine Shear Zone (RSSZ) and Hyde-Macraes Shear Zone (HMSZ). After Deckert et al. 2002. (C) Generalized regional geology map of the area around Tucker Hill after Barker, 2005. (D) Map showing key structural geatures and measurements made at Tucker Hill, and the location of the sample collected for geochronology, after Barker, 2002.

Fig. 2: (A) Typical thick (c. 1 cm thick) pseudotachylyte vein in outcrop formed of schist host rock. Pen (15 cm long) for scale, with pseudotachylyte vein at pen tip. (B) Thickest pseudotachylyte vein found at Tucker Hill (c. 5 cm thick) examined in thin section. Note several sets of chill margins and quartz lithic clasts. Ruler (cm markings) for scale. (C) Photomicrograph showing a typical margin of a pseudotachylyte vein. Note numerous lithic clasts, especially in margin of vein. Tiny potassium feldspar microlites (10 μm scale) can be seen in to right side of photomicrograph, away from chill margin.

Fig. 3: (A) SEM backscattered electron photomicrograph showing a typical fractured quartz lithic clast. Note lighter grey melt phase infilling crack, and barren crack (darkest grey, from top of lithic clast). (B) Photomicrograph in plane polarised light showing a blurry rimmed lithic clast, surrounded by a fine-grained matrix composed mainly of chlorite. (C) SEM photomicrograph showing an indistinct rimmed plagioclase lithic clast, onto which potassium feldspar microlites are growing. Chlorite forms the majority of the surrounding matrix material.

Fig. 4: TEM brightfield photomicrograph showing a mat of fine-grained chlorite in a matrix area of pseudotachylyte.

Figure 5: (A) Photomicrograph in plane polarised light showing spheroids in OU 74178. Note dark black graphite rim on edge of spheroids, and titanite growing from edges of spheroid towards centre. (B) SEM backscattered electron photomicrograph showing radial morphology of a titanite grain contained within an spheroid. Titanite appears to nucleate from a point to the bottom right of photomicrograph. (C) Photomicrograph in plane polarised light showing spheroids in OU 74178. Note zoning within titanites, and both quartz (dominant infilling material in large, central spheroid) and potassium feldspar (right hand side of large, central spheroid).

Figure 6: (A) Comparison of pseudotachylyte and schist major element XRF compositions, calculated as R, the ratio of a trace element in pseudotachylyte compared to schist. To illustrate the size and significance of these compositional variations between pseudotachylyte and host schist concentration ratios have been calculated with errors included using standard propagation techniques (see text for details). (B) Comparison of pseudotachylyte and schist trace element X-ray fluorescence composition. Note depletions in Ga, As, Sr and Y, and enrichments in Rb, Ba and Nb (in pseudotachylyte relative to schist).

Figure 7: (A) Comparison of pseudotachylyte and schist trace element compositions as determined by laser ablation, inductively couple plasma mass spectrometry. Note Rb and Ba

enrichments, and significant depletions in Sr and Eu. (B) Chrondite normalised REE plot of schist and pseudotachylyte (as determined by LA-ICP-MS). Note significant Eu anomaly, which is only present in pseudotachylyte.

Figure 8: (A) Ar-Ar age spectra for encapsulated stepwise heated sample of "intact rock" pseudotachylyte matrix. (B) Ar-Ar age spectra for unencapsulated stepwise heated sample of pseudotachylyte matrix.

Figure 9: Thin section of OU 74177 displaying flow banding (section length 50 mm).

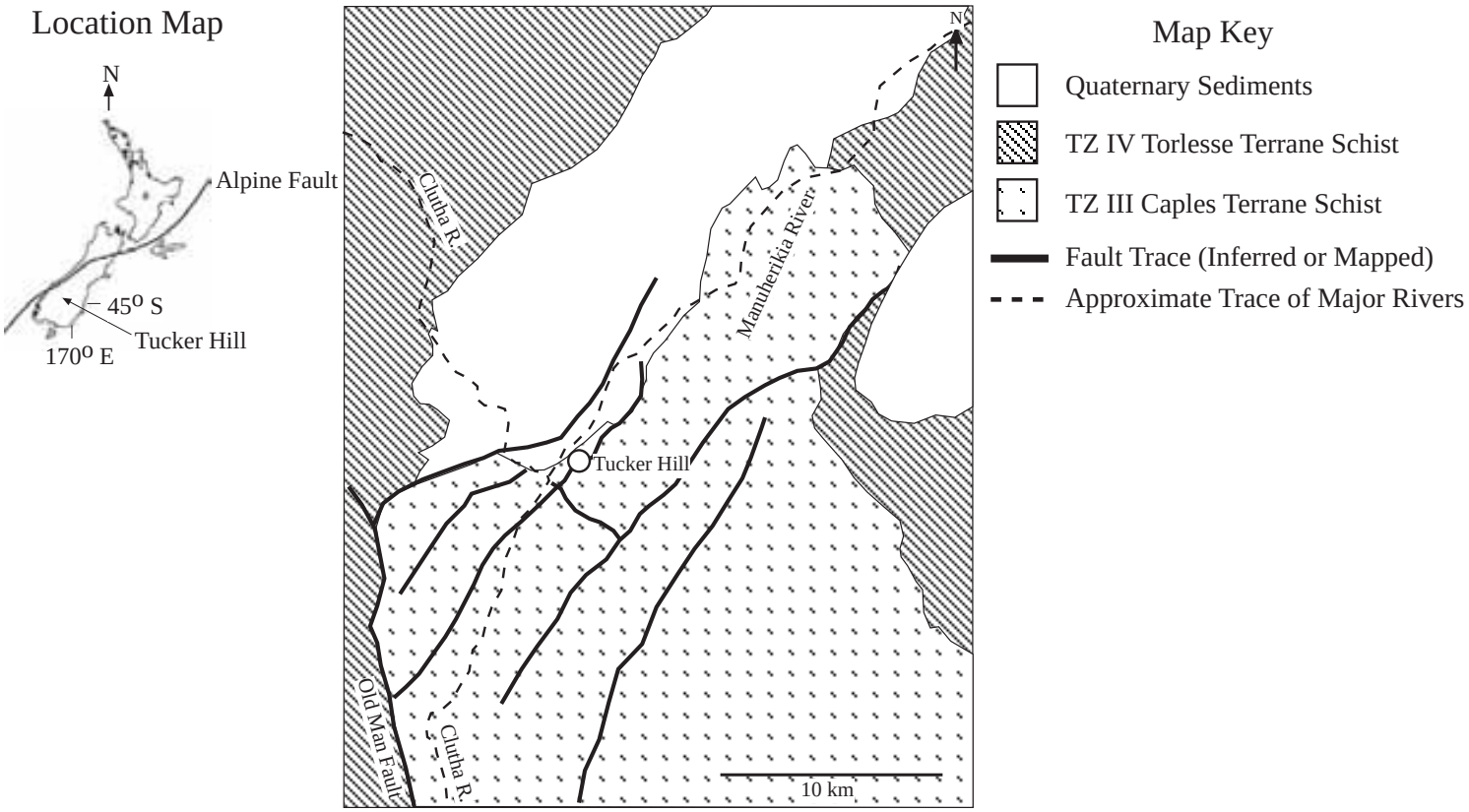

Figure 1a

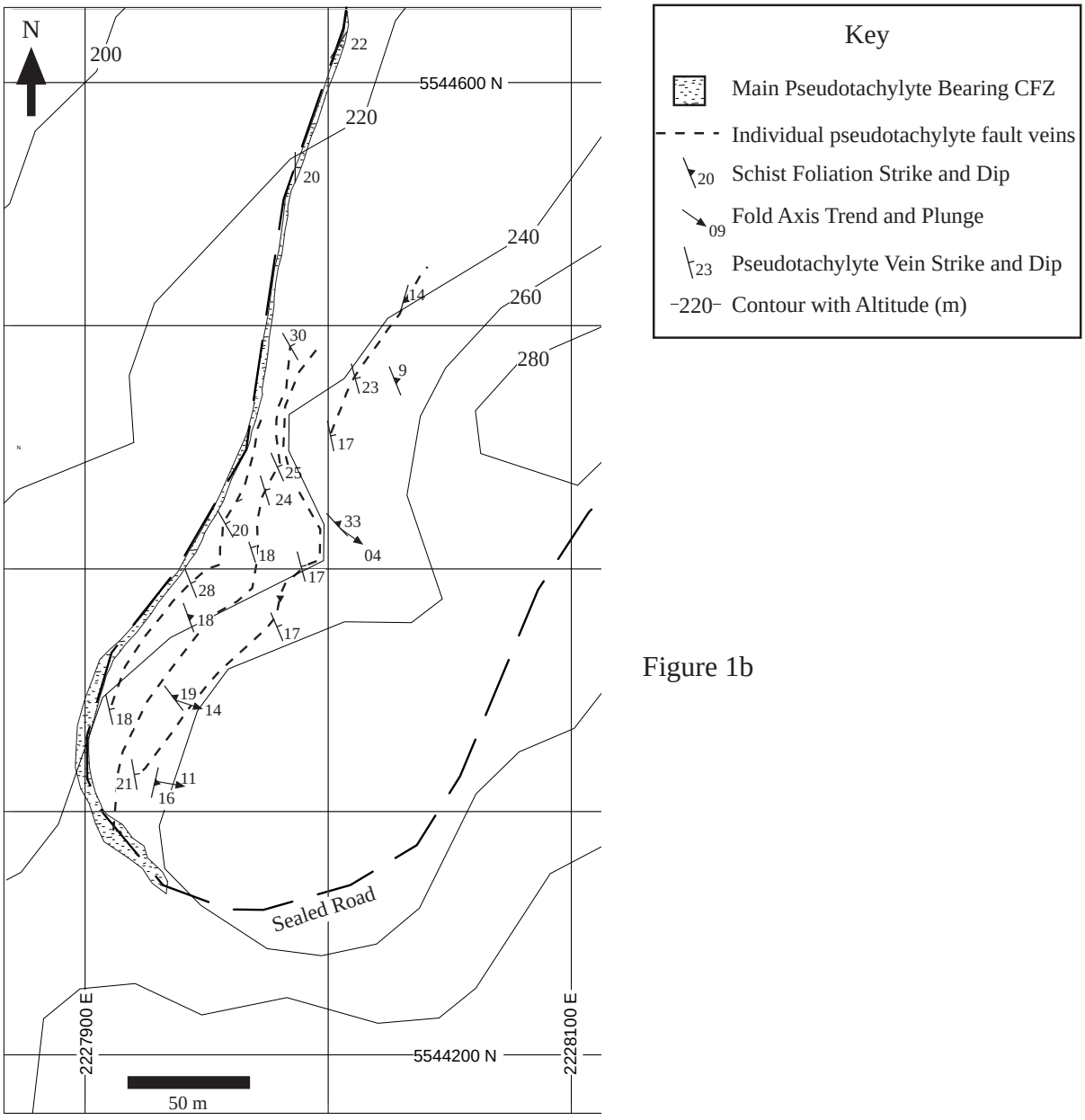

Figure 1b

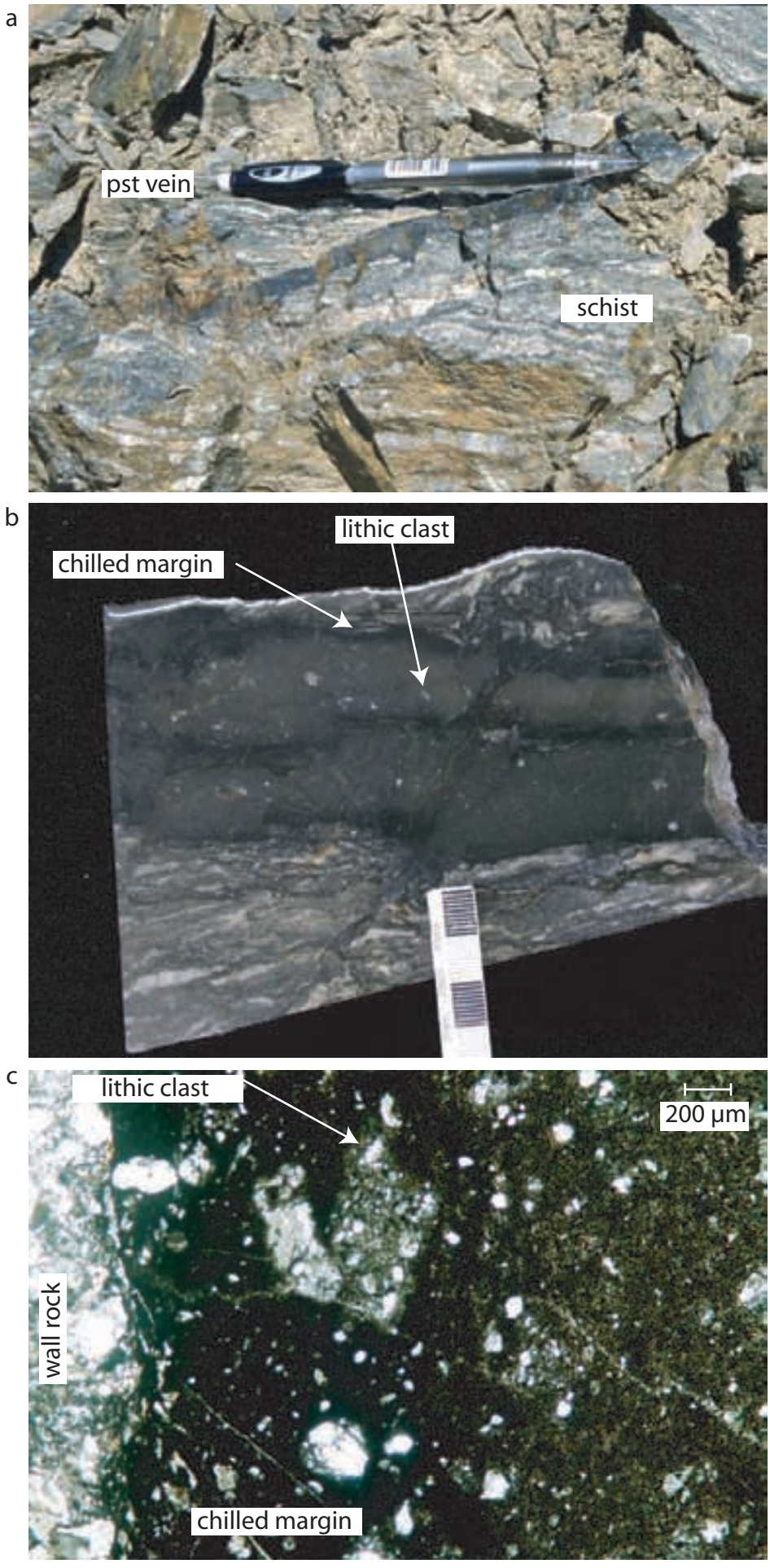
a
pst vein
schist
b
lithic clast
chilled margin
c
lithic clast
200 µm
wall rock
chilled margin

Figure 2

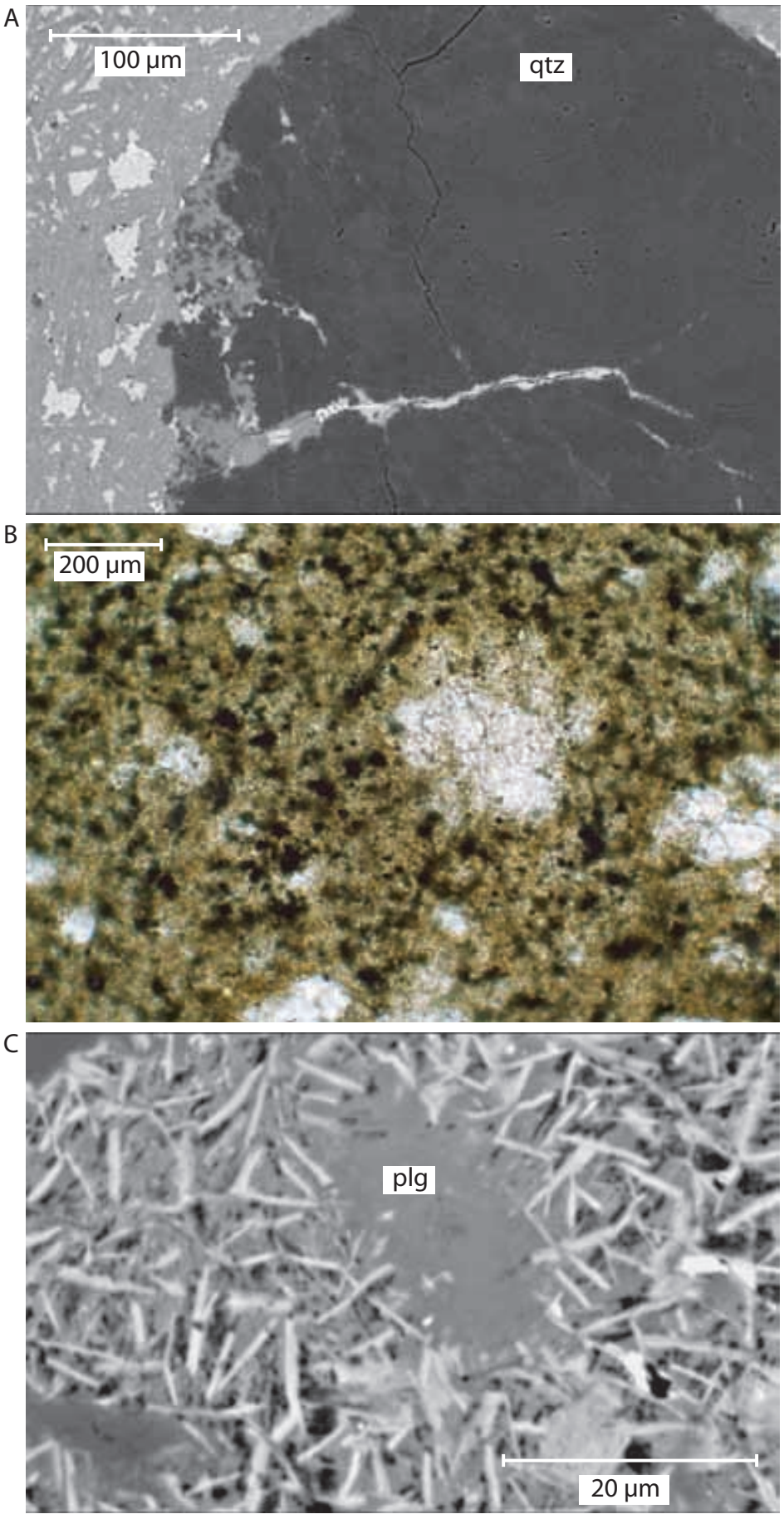

Figure 3

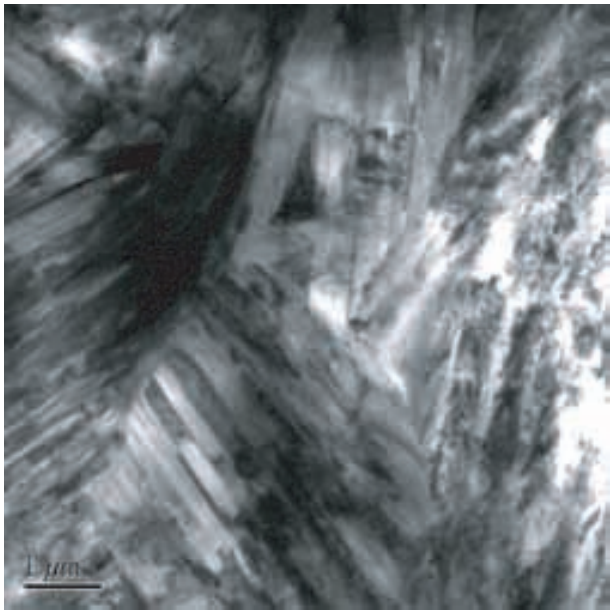

Figure 4

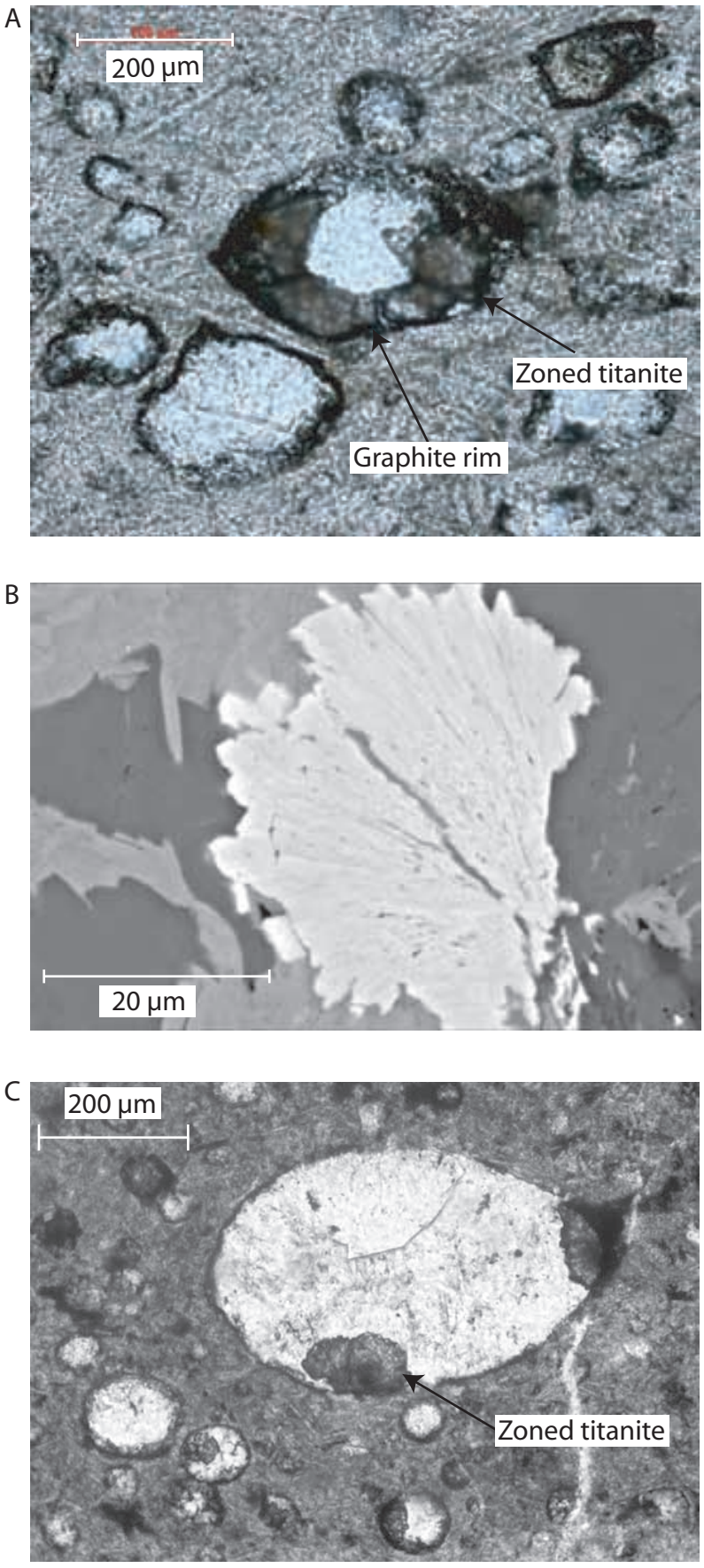
A
200 µm
Zoned titanite
Graphite rim
B
20 µm
C
200 µm
Zoned titanite

Figure 5

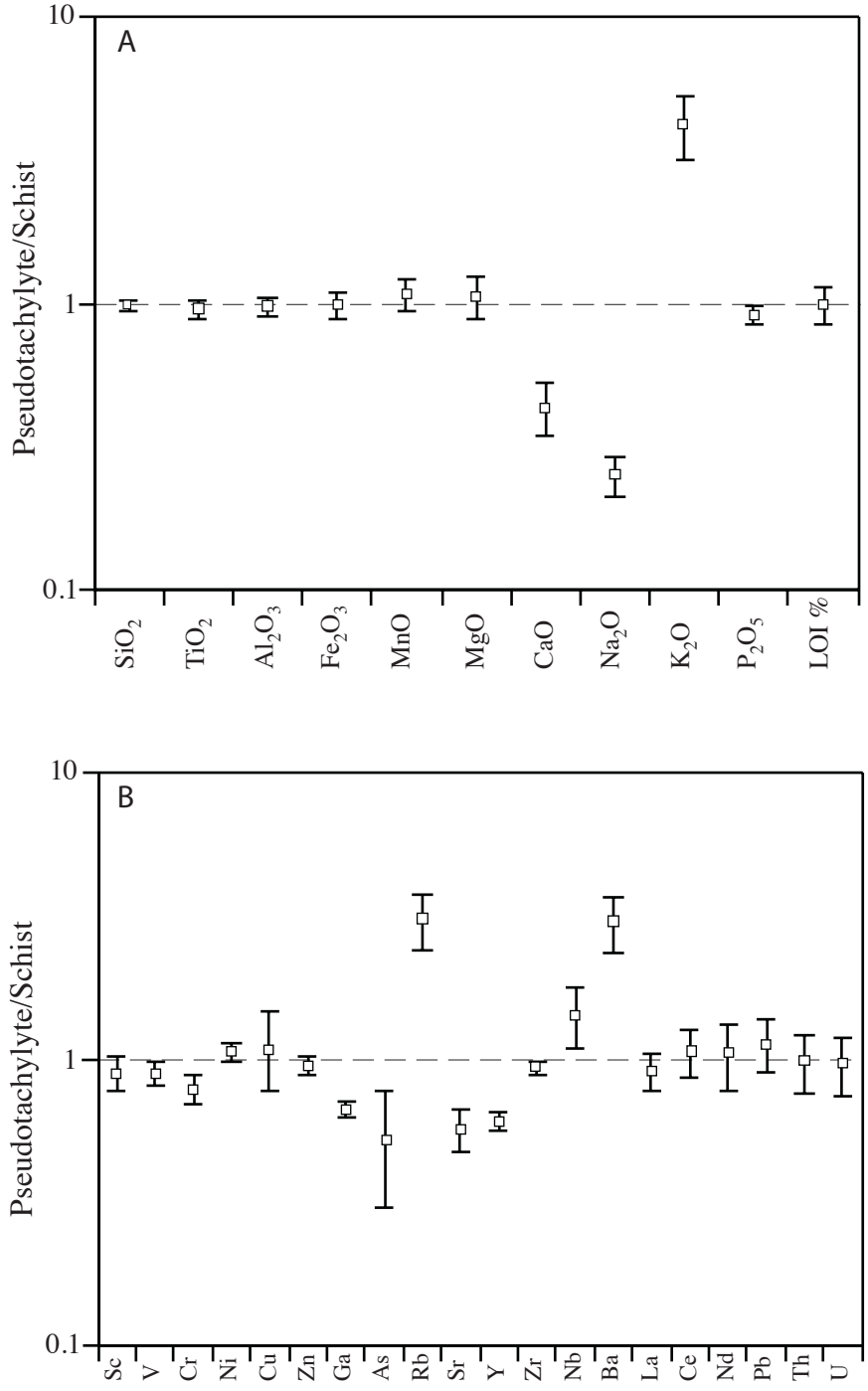
A
10
1
0.1
Pseudotachylyte/Schist
SiO2
TiO2
Al2O3
Fe2O3
MnO
MgO
CaO
Na2O
K2O
P2O5
LOI %
B
10
1
0.1
Pseudotachylyte/Schist
Sc
V
Cr
Ni
Cu
Zn
Ga
As
Rb
Sr
Y
Zr
Nb
Ba
La
Ce
Nd
Pb
Th
U

Figure 6

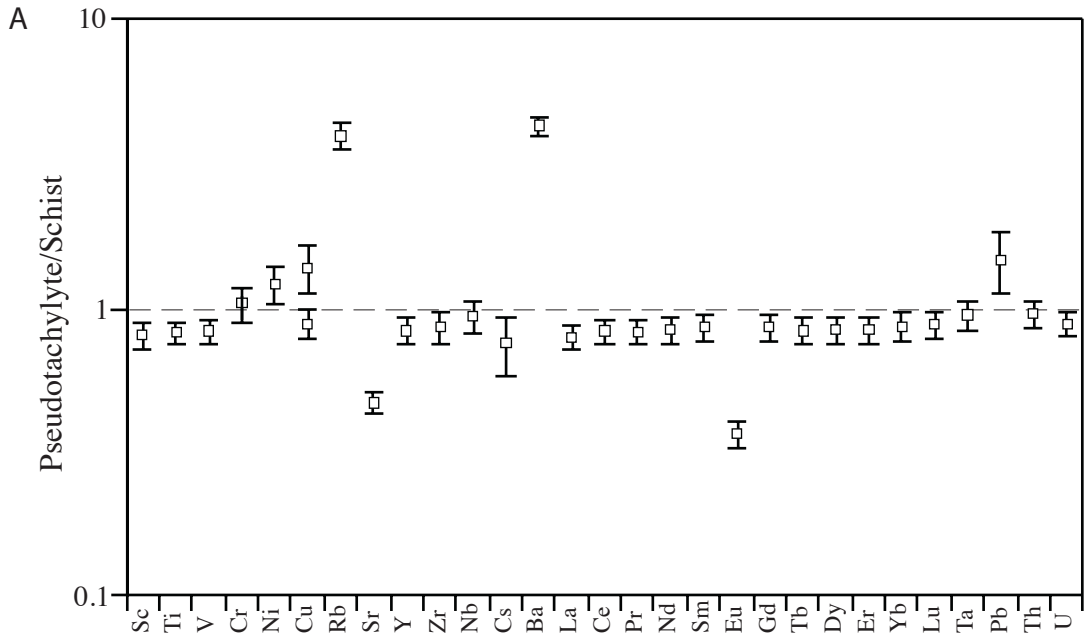
A
10
1
0.1
Pseudotachylyte/Schist
Sc
Ti
V
Cr
Ni
Cu
Rb
Sr
Y
Zr
Nb
Cs
Ba
La
Ce
Pr
Nd
Sm
Eu
Gd
Tb
Dy
Er
Yb
Lu
Ta
Pb
Th
U

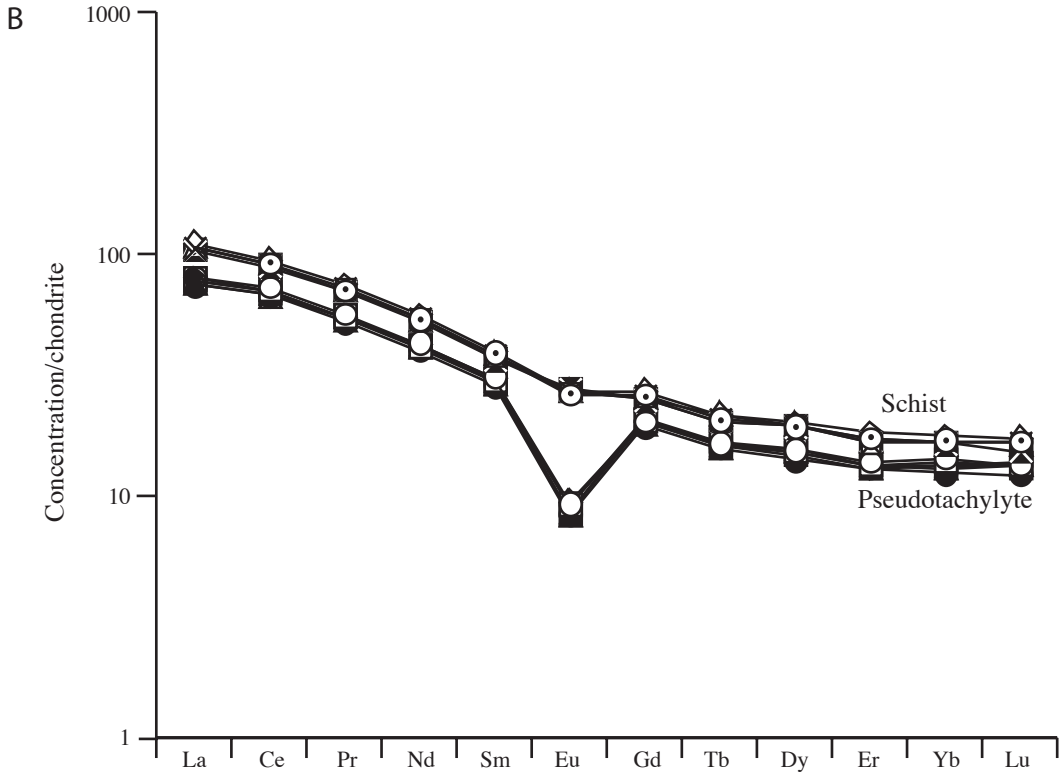
B
1000
100
10
1
Concentration/chondrite
Schist
Pseudotachylyte
La
Ce
Pr
Nd
Sm
Eu
Gd
Tb
Dy
Er
Yb
Lu

Figure 7

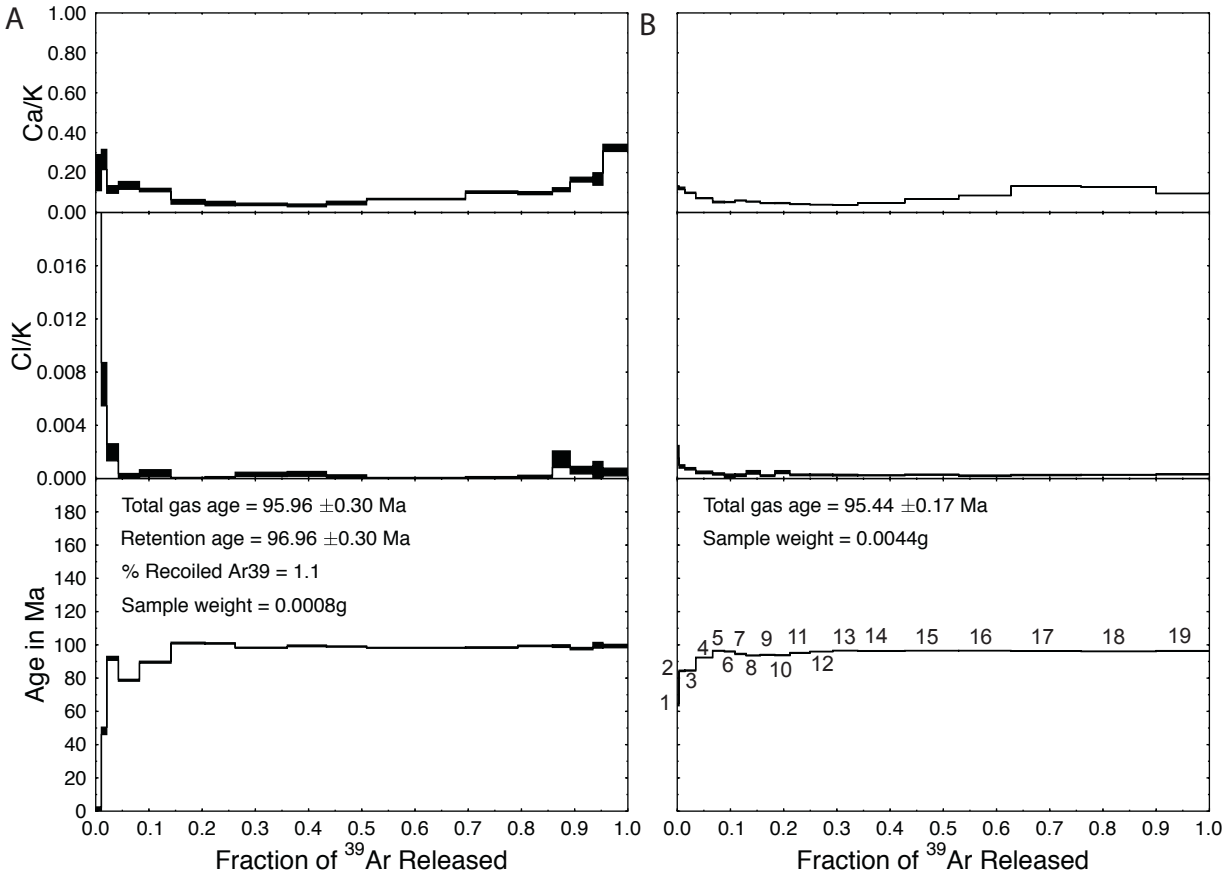
A
B
Ca/K
Cl/K
Age in Ma
Total gas age = 95.96 ±0.30 Ma
Retention age = 96.96 ±0.30 Ma
% Recoiled Ar39 = 1.1
Sample weight = 0.0008g
Total gas age = 95.44 ±0.17 Ma
Sample weight = 0.0044g
Fraction of ^{39}Ar Released
Fraction of ^{39}Ar Released

Figure 8

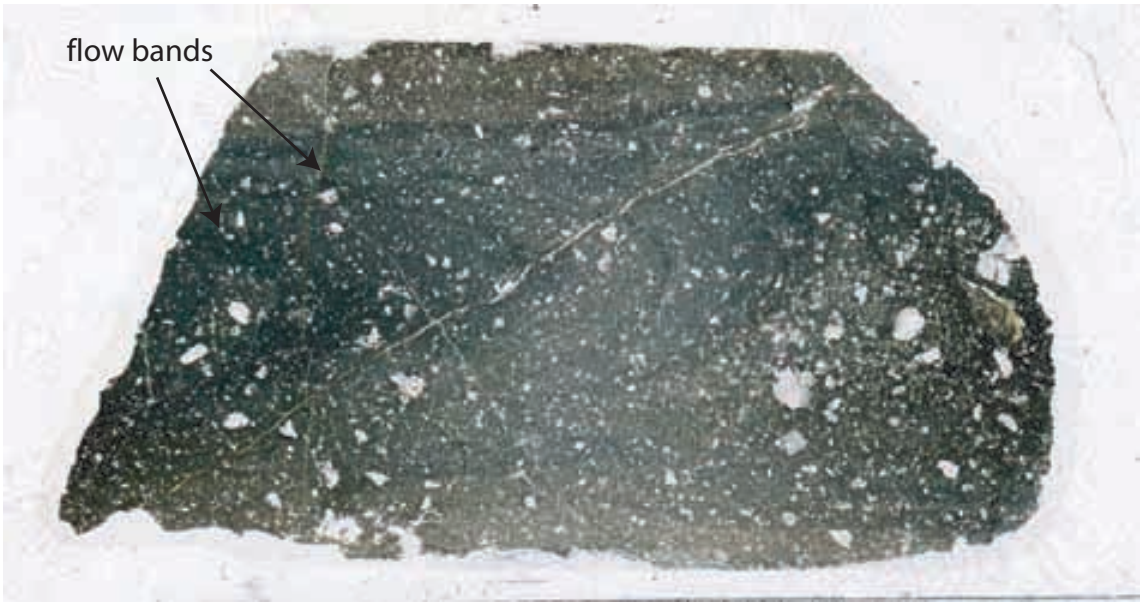

Figure 9